Efficient Analysis of Arbitrarily Shaped Inductive Obstacles in Rectangular Waveguides Using a Surface Integral Equation Formulation

Fernando D. Quesada Pereira [1], Vicente E. Boria Esbert [2], *Senior Member, IEEE,* Juan Pascual García [1], Ana Vidal Pantaleoni [2], *Member, IEEE,* Alejandro Alvarez Melcón [1], *Member, IEEE,* J.L. Gomez Tornero [1], and Benito Gimeno [3], *Member, IEEE,*

***Abstract*— In this paper we propose to use the Surface Integral Equation technique for the analysis of arbitrarily shaped H-plane obstacles in rectangular waveguides, which can contain both metallic and/or dielectric objects. The Green functions are formulated using both spectral and spatial images series, whose convergence behavior has been improved through several acceleration techniques. Proceeding in this way, the convergence of the series is not attached to the employment of any particular basis or test function, thus consequently increasing the flexibility of the implemented technique. In order to test the accuracy and numerical efficiency of the proposed method, results for practical microwave circuits have been successfully compared with other numerical approaches.**

***Index Terms*— Waveguide components, Waveguide discontinuities, Dielectric resonators, Integral equations, Green functions, Moment methods.**

I. Introduction

THE analysis and design of rectangular waveguide devices based on inductive obstacles is a subject extensively treated in the technical literature, due to their wide use in space and ground telecommunications applications [1]-[4]. For the analysis of these problems, equivalent circuit techniques were successfully derived in the past [5]. More recently, full-wave mode-matching methods [6]-[8] have been successfully applied to cope with this kind of problems. However, for design purposes, more efforts should be devoted in order to improve the numerical efficiency of such analysis techniques, while preserving accuracy issues at the same time. To reach this aim, the Integral Equation (IE) technique can be considered as a good alternative analysis method.

For instance, in [9], an IE method was used to derive equivalent circuits for a single metallic inductive square post. The analysis of an arbitrary number of metallic posts inside rectangular waveguides has also been the subject of other classical works [10]-[12], where different IE approaches were successfully proposed. In these methods, the Parallel Plate Waveguide (PPW) Green functions were used to reduce the numerical solution of the inductive problem. However, the PPW Green functions consists of slowly convergent infinite series, either in the spatial or in the spectral domain. To accelerate the convergence rate of such series, the Kummer's transformation was applied in [10] and [12], whereas particular choices of basis functions were successfully proposed in [11]. Nevertheless, the flexibility on the kind of geometries that could be treated in all such works was widely reduced.

Later on, several extensions of previous IE methods for dealing with multiple dielectric obstacles were reported. For instance, in [13], a volume IE method solved by the Method of Moments (MoM) was successfully applied to the analysis of multiple dielectric posts. Band-pass and band-rejection filters based on two dielectric posts were fully designed in [14]. More recently, the IE technique is also being proposed for dealing with cavity filters loaded with dielectric and metallic posts [15], [16]. However, further research on improving the flexibility and numerical efficiency of IE-based methods is needed for Computer-Aided Design (CAD) purposes.

In this paper, the authors propose a very efficient surface IE technique for the accurate analysis of arbitrarily shaped inductive waveguide structures, which can be composed of any number of conducting and/or dielectric obstacles. A detailed study of the convergence behavior of both spatial and spectral domain series is presented, and new improvements regarding the fast evaluation of the PPW Green functions and their spatial derivatives are proposed. This new approach allows the use of triangular functions in the MoM solution of the corresponding IEs, thus increasing the accuracy of the final results, as well as the complexity of the geometries that can be considered. Several waveguide devices of great practical interest, such as rod microwave filters and lossy dielectric loaded filters including mechanization effects (i.e. the typical rounded corners effects), have been successfully considered for verification purposes.

II. Theory

Conducting and dielectric inductive obstacles placed within a rectangular waveguide, as shown in Fig. 1, can be studied using the surface equivalence principle [17]. For the sake of simplicity, the basic formulation is written for the structure shown in Fig. 1, where only one homogeneous dielectric body with permittivity ϵ_1, and one perfect conductor are placed

[1]Technical University of Cartagena, Campus Muralla del Mar s/n, Cartagena, E-30202, Spain, E-mail: fernando.quesada@upct.es.

[2] Technical University of Valencia, Camino de Vera s/n, Valencia, E-46022, Spain, E-mail:vboria@dcom.upv.es

[3] University of Valencia, Burjasot, Valencia E-46100, Spain, E-mail:benito.gimeno@uv.es

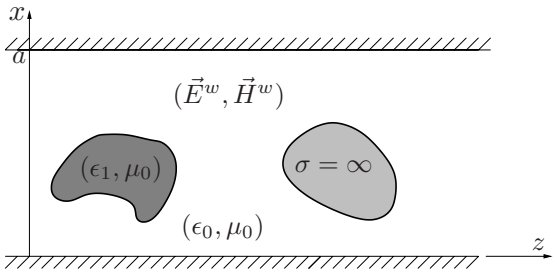

Fig. 1. Typical inductive geometry considered in this paper, which contains metallic and dielectric obstacles.

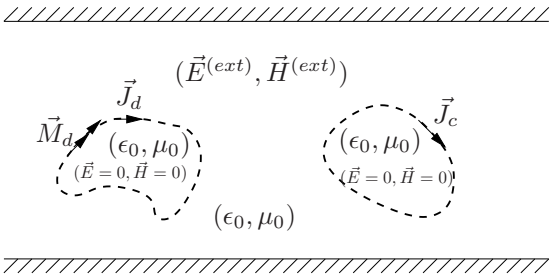

Fig. 2. External problem after applying the surface equivalence principle.

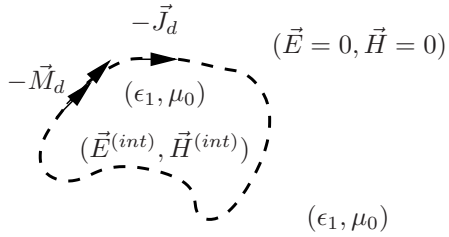

Fig. 3. Internal problem once the surface equivalence principle is applied.

together within the waveguide. As shown in the figure, both the dielectric and the metallic obstacles are of arbitrary geometry. This formulation, presented next, can be easily extended in a very straightforward way in order to account for any arbitrary number of conductors and/or dielectric obstacles.

The surface equivalence principle allows to replace the original problem shown in Fig. 1 by two different coupled equivalent problems [17]. The first one, shown in Fig. 2, is the equivalent problem formulated in the region outside the inductive obstacles (also called external problem). In this case, the inductive posts are replaced by their equivalent electric ($\vec{J}_d$, $\vec{J}_c$) and magnetic ($\vec{M}_d$) surface current densities, which radiate in a rectangular waveguide filled with air (ϵ_0, μ_0). In the second equivalent problem (also called internal problem), the surface electric and magnetic equivalent current densities ($-\vec{J}_d$, $-\vec{M}_d$) radiate (in the absence of the original sources) inside the dielectric homogenous body of permittivity constant ϵ_1 (see Fig. 3). It is worth mentioning that the internal problem does not have to be considered for the perfect conducting bodies, since the fields are zero inside a perfect conductor.

For the external problem, the total electric and magnetic fields ($\vec{E}^{(ext)}$,$\vec{H}^{(ext)}$) inside the waveguide are due to the fields impressed by the excitation ($\vec{E}^i$,$\vec{H}^i$), together with the fields scattered by the inductive posts ($\vec{E}^s$,$\vec{H}^s$). For the inductive problems under consideration, we will assume that the fundamental rectangular waveguide TE_{10} mode excites the structure. Then, the total field for the external problem is:

$$\vec{E}^{(ext)} = \vec{E}^s_{ext}(\vec{J}_d, \vec{M}_d, \vec{J}_c) + \vec{E}^i \tag{1a}$$

$$\vec{H}^{(ext)} = \vec{H}^s_{ext}(\vec{J}_d, \vec{M}_d, \vec{J}_c) + \vec{H}^i \tag{1b}$$

For the internal problem, the total fields ($\vec{E}^{(int)}$,$\vec{H}^{(int)}$) are only due to the radiation of the equivalent surface currents on the homogeneous medium:

$$\vec{E}^{(int)} = \vec{E}^s_{int}(-\vec{J}_d, -\vec{M}_d) \tag{2a}$$

$$\vec{H}^{(int)} = \vec{H}^s_{int}(-\vec{J}_d, -\vec{M}_d) \tag{2b}$$

In both cases, the electric and magnetic fields will be expressed for numerical convenience in terms of the mixed potentials, as it is suggested in [18].

The proposed IE technique is based on the imposition of the boundary conditions for the electromagnetic fields. For the conducting bodies, a zero tangent component for the electric field is enforced. For the dielectric materials we impose the continuity of the tangential components of the total electric and magnetic fields across the surfaces. This leads to the so called Poggio-Miller-Chang-Harrington-Wu-Tsu (PMCHWT) formulation [19]. After imposing such boundary conditions, a system of three coupled integral equations is obtained:

$$\begin{aligned}\hat{n} \times \bar{E}^i(\bar{\rho}) = \hat{n} \times \Bigg\{ & j\,\omega \left[\overline{\overline{G}}_A^{(ext)} + \overline{\overline{G}}_A^{(int)}\right] \otimes \bar{J}_d \\ & -\frac{1}{j\,\omega}\nabla\left[\left(G_V^{(ext)} + G_V^{(int)}\right) \otimes \left(\nabla' \cdot \bar{J}_d\right)\right] \\ & +\frac{1}{\epsilon_0}\nabla \times \left[\overline{\overline{G}}_F^{(ext)} \otimes \bar{M}_d\right] + \frac{1}{\epsilon_1}\nabla \times \left[\overline{\overline{G}}_F^{(int)} \otimes \bar{M}_d\right] \\ & +j\,\omega\left[\overline{\overline{G}}_A^{(ext)} \otimes \bar{J}_c\right] - \frac{1}{j\,\omega}\nabla\left[G_V^{(ext)} \otimes \left(\nabla' \cdot \bar{J}_c\right)\right] \Bigg\}_{S_d}\end{aligned} \tag{3}$$

$$\begin{aligned}\hat{n} \times \bar{H}^i(\bar{\rho}) = \hat{n} \times \Bigg\{ & -\frac{1}{\mu_0}\nabla \times \left[\overline{\overline{G}}_A^{(ext)} \otimes \bar{J}_d\right] \\ & -\frac{1}{\mu_0}\nabla \times \left[\overline{\overline{G}}_A^{(int)} \otimes \bar{J}_d\right] + j\,\omega\left(\overline{\overline{G}}_F^{(ext)} + \overline{\overline{G}}_F^{(int)}\right) \otimes \bar{M}_d \\ & -\frac{1}{j\,\omega}\nabla\left[\left(G_W^{(ext)} + G_W^{(int)}\right) \otimes \left(\nabla' \cdot \bar{M}_d\right)\right] \\ & -\frac{1}{\mu_0}\nabla \times \left[\overline{\overline{G}}_A^{(ext)} \otimes \bar{J}_c\right] \Bigg\}_{S_d}\end{aligned} \tag{4}$$

$$\hat{n}\times\bar{E}^{i}(\bar{\rho})=\hat{n}\times\Bigg\{j\,\omega\left(\overline{\overline{G}}_{A}^{(ext)}\otimes\bar{J}_{d}\right)$$
$$-\frac{1}{j\,\omega}\,\nabla\left[G_{V}^{(ext)}\otimes\left(\nabla'\cdot\bar{J}_{d}\right)\right]+\frac{1}{\epsilon_{0}}\,\nabla\times\left[\overline{\overline{G}}_{F}^{(ext)}\otimes\bar{M}_{d}\right]$$
$$+j\,\omega\left(\overline{\overline{G}}_{A}^{(ext)}\otimes\bar{J}_{c}\right)-\frac{1}{j\,\omega}\nabla\left[G_{V}^{(ext)}\otimes\left(\nabla'\cdot\bar{J}_{c}\right)\right]\Bigg\}_{S_{c}} \tag{5}$$

where the symbol "$\otimes$" denotes a superposition (convolution) integral [17], the "(ext)" superscript denotes the PPW Green functions of the external problem, and "(int)" means the Green functions of an unbounded homogeneous medium with constitutive parameters ϵ_1 and μ_0. For this interior problem, the Green functions are formulated as simple Hankel functions of second kind [20], while for the exterior problem the PPW Green functions will be used. In (3), vector $\hat{n}$ is the outgoing unitary normal vector to each obstacle contour.

The previous system of IEs has been numerically solved following the well-known Galerkin-MoM technique. In this work, the unknown current surface densities ($\bar{J}_d(\rho')$, $\bar{M}_d(\rho')$ and $\bar{J}_c(\rho')$) are expanded in terms of subsectional triangular basis functions [17]. The use of triangular functions can be easily accomplished with this formulation, since the Green's functions are directly obtained in the spatial domain. This strategy is useful for the analysis of complex shaped structures, and it is not possible in other spectral domain approaches [11].

Due to the invariance along the y-axis of the inductive problems under study, there is no contribution from the electric scalar potential. On the other hand, the gradient of the magnetic scalar potential is transferred to the testing functions, thus avoiding the calculation of such Green function derivatives. However, the curl of the magnetic and electric vector potentials can not be transferred to the divergence conforming testing functions used in this work. As a consequence, the evaluation of the spatial derivatives of the Green functions can not be avoided for the curl operator. In order to speed up the numerical evaluation of all Green functions and derivatives, we will study next their convergence properties, and then we will derive a novel strategy for the efficient evaluation of the required series.

A. PPW Green Functions Convergence

The PPW Green functions in the structure shown in Fig. 4 can be formulated using the classical theory of images with respect to two infinite parallel metallic plates [20]. In this case, the scalar Green's function is expressed with the following spatial image series:

$$G_{Spat}^{(ext)}(x,x',z-z')=\sum_{n=-\infty}^{+\infty}\Big[G(x,+x'+2na,z-z')+$$
$$s_g\,G(x,-x'+2na,z-z')\Big] \tag{6}$$

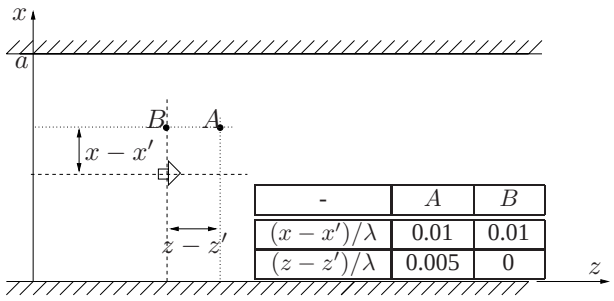

-	A	B
$(x-x')/\lambda$	0.01	0.01
$(z-z')/\lambda$	0.005	0

Fig. 4. Source and observer points locations in a PPW used in the convergence study ($a/\lambda = 0.75$).

where

$$G(x,x',z-z')=\frac{\xi}{j\,4}\,H_0^{(2)}(k_0\,\rho), \tag{7a}$$
$$\rho=\sqrt{(x-x')^2+(z-z')^2} \tag{7b}$$

s_g is the sign function (see Table I), and ξ is a constitutive parameter taking the values shown in Table I for the different Green function components.

TABLE I

VALUES OF THE PARAMETERS IN EQUATIONS (6), (7) AND (9) FOR ALL RELEVANT GREEN FUNCTIONS COMPONENTS.

-	s_g	ξ	f_n	g_n
$G_A^{(ext)}$	-1	μ_0	$\sin(k_x\,x)$	$\sin(k_x\,x')$
$G_W^{(ext)}$	$+1$	$1/\epsilon_0$	$\cos(k_x\,x)$	$\cos(k_x\,x')$

The spectral formulation of the PPW Green functions is related to the spatial image series through the Poisson's summation formula [21]:

$$\sum_{n=-\infty}^{+\infty}f(2na)=\frac{\sqrt{2\pi}}{2a}\sum_{n=-\infty}^{+\infty}\tilde{f}(n\pi/a) \tag{8}$$

where $(\tilde{f})$ denotes the Fourier transformation of (f). Applying the above transformation, the spectral series takes the following general expression:

$$G_{Spec}^{(ext)}(x,x',z-z')=\frac{2}{a\,\pi}\sum_{n=0}^{\infty}\tilde{G}(k_x,z-z')\,f_n(k_x\,x)\;g_n(k_x\,x') \tag{9}$$

where f_n and g_n are harmonic functions taking the form shown in Table I for the different Green functions components, and the Fourier transformation of the Hankel function is:

$$\tilde{G}(k_x,z-z')=\xi\;\frac{e^{-j\,k_z\,|z-z'|}}{j\,k_z}, \tag{10a}$$
$$k_z=\sqrt{k_0^2-k_x^2},\qquad k_x=\frac{n\,\pi}{a}. \tag{10b}$$

Due to the exponential behavior of this last expression, the convergence of the modal series is fast for large $|z-z'|$ distances. On the contrary, the spatial images series in (6) exhibits much slower convergence behavior.

As it was introduced before, the curl operator of (3)-(5) results in the spatial derivatives of the Green functions. When the spatial images formulation is used, the corresponding

derivatives only affect the Hankel term of the Green function shown in (7a), which after simple calculations give place to the following expressions:

$$\frac{\partial G(x,x',z-z')}{\partial x} = -\frac{\xi}{j\,4}\,k_0\;(x-x')\;\frac{H_1^{(2)}(k_0\,\rho)}{\rho} \tag{11a}$$

$$\frac{\partial G(x,x',z-z')}{\partial z} = -\frac{\xi}{j\,4}\,k_0\;(z-z')\;\frac{H_1^{(2)}(k_0\,\rho)}{\rho} \tag{11b}$$

where now, the Hankel function of order one must be used inside the series representation of equation (6).

From the above expressions, we can readily notice the additional convergence factor due to the distance from the source point to the observation point (ρ), which appears in the denominator. However, for the derivative along the x-axis, this additional (ρ) term is compensated with the $(x-x')$ factor in the numerator. In fact, when the images distance increases, the global term $[(x-x')/\rho]$ tends to one. Therefore, convergence is only due to the first order Hankel function. A different situation appears for the derivative along the z-axis. In this case, the factor $(z-z')$ remains constant when the distance of the images is increased. Consequently, the additional (ρ) term results in a very important convergence rate improvement.

When similar derivatives are applied to the spectral representation of the series shown in (9), the following final expressions are obtained:

$$\frac{\partial G^{(ext)}(x,x',z-z')}{\partial x} = +\frac{2}{a\pi}\sum_{n=0}^{\infty}\tilde{G}(k_x,z-z')\,k_x\,f_n(k_x\,x)\;g_n(k_x\,x') \tag{12a}$$

$$\frac{\partial G^{(ext)}(x,x',z-z')}{\partial z} = -\frac{2}{a\pi}\sum_{n=0}^{\infty}\tilde{G}(k_x,z-z')\,j\,k_z\,f_n(k_x\,x)\;g_n(k_x\,x') \tag{12b}$$

where the spectral Green function ($\tilde{G}$) is the same as in (10a), and the new harmonic functions change into the form shown in Table II for each corresponding component.

TABLE II

VALUES OF THE PARAMETERS IN EQUATIONS (10) AND (12), FOR THE SPATIAL DERIVATIVES OF THE GREEN'S FUNCTIONS.

-	ξ	f_n	g_n
$\frac{\partial G_A^{(ext)}}{\partial x}$	μ_0	$\cos(k_x\,x)$	$\sin(k_x\,x')$
$\frac{\partial G_W^{(ext)}}{\partial x}$	$1/\epsilon_0$	$-\sin(k_x\,x)$	$\cos(k_x\,x')$
$\frac{\partial G_A^{(ext)}}{\partial z}$	μ_0	$\sin(k_x\,x)$	$\sin(k_x\,x')$

In this case, we can notice that convergence is degraded by the new spectral factors introduced by the derivatives. Therefore, a slower convergence rate is expected for the Green functions derivatives using the spectral formulation.

In order to increase the convergence rate of the spectral series, the use of the Kummer transformation is proposed (see [10] and [22]). In Appendix I we extend the Kummer formulation to all Green functions and their spatial derivative components that appear following the surface integral equation derived in this paper. Now we perform a convergence behavior study after application of the Kummer's transformation to the spectral domain formulation. In Fig. 5 and Fig. 6, we present the relative errors obtained for the basic Green function components when the observer point is located at positions A and B (see Fig. 4). If we compare the behavior with the image series, we observe that convergence rate is strongly improved for observer point A. Now, even for the B observer point (placed at the critical plane $z=z'$), the spectral domain series surpass largely the spatial images counterpart. By means of the employment of the Kummer's transformation, a good convergence behavior can be obtained at all points of the geometry (relative errors below 10^{-5} are always obtained with less than 100 modes).

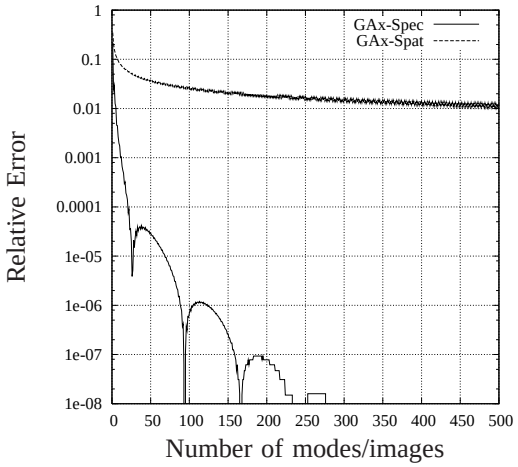

Fig. 5. Convergence of the spectral domain series after application of the Kummer's transformation. Convergence of spatial domain series are presented for comparison. Observer point at position A.

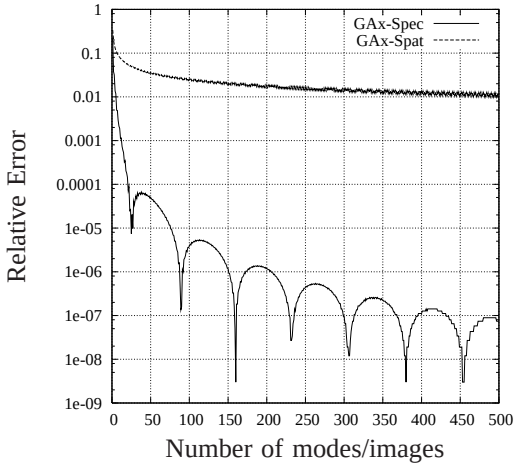

Fig. 6. Convergence of the spectral domain series after application of the Kummer's transformation. Convergence of spatial domain series are presented for comparison. Observer point at position B.

To complete the study, we present in Fig. 7 and Fig. 8 similar convergence results, but now for the relevant spatial derivatives. With respect to the z-spatial derivative, we

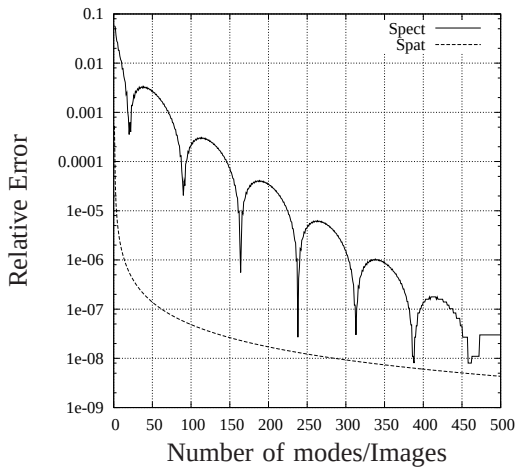

Fig. 7. Convergence of the spectral domain spatial derivatives series after application of the Kummer transformation. Convergence of spatial domain series for the derivatives are presented for comparison. Observer point at position A; spatial derivatives with respect to the z-axis.

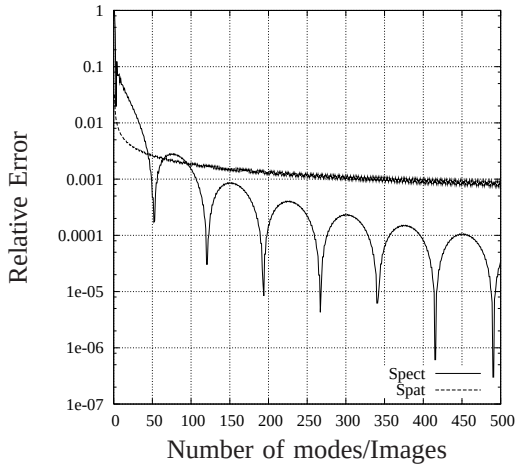

Fig. 8. Convergence of the spectral domain spatial derivatives series after application of the Kummer's transformation. Convergence of spatial domain series for the derivatives are presented for comparison. Observer point at position B; spatial derivatives with respect to the x-axis.

observe in Fig. 7 that the images series exhibits an impressive convergence behavior (only 15 images are needed to obtain a relative error of 10^{-5}). Therefore, the spatial images series is preferred for the z-axis spatial derivative over the spectral representation. On the other hand, Fig. 8 shows that the Kummer technique is slightly better that the images series for the x-axis spatial derivative evaluated at the critical point B ($|z - z'| = 0$). In this case, a relative error of 10^{-3} can be obtained with 100 modes, using the Kummer transformation. If lower errors are needed for a particular application, other acceleration techniques can still be used, such as the Ewald method [23].

From this convergence study, we can conclude that the PPW Green functions and their spatial derivatives will be evaluated using the spectral representation of the series, in combination with the Kummer transformation. This is the general rule, except for the z-derivatives of the Green functions at points satisfying the condition: $|z - z'|/\lambda < 0.02$. We have seen

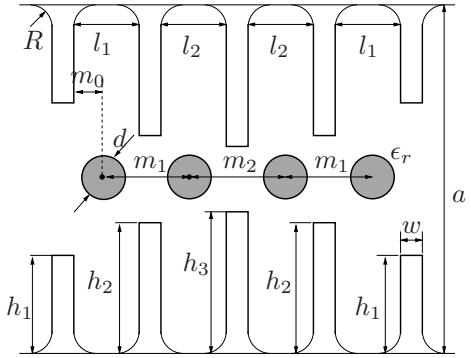

Fig. 9. Fourth order dielectric loaded inductive filter. The dimensions are: $a = 19.05$ mm, $w = 2$ mm, $d = 4.0$ mm, $\epsilon_r = 2$, $h_1 = 4.725$ mm, $h_2 = 6.405$ mm, $h_3 = 6.595$ mm, $l_1 = 12.03$ mm, $l_2 = 13.62$ mm, $m_0 = 6.015$ mm, $m_1 = 14.815$ mm and $m_2 = 15.600$ mm, $R = 2.5$ mm.

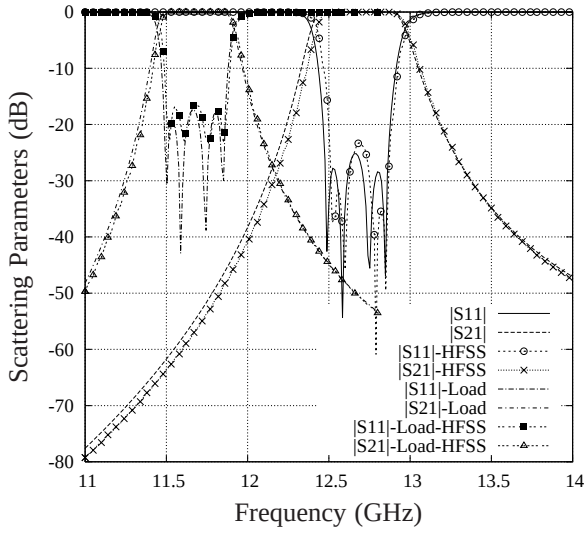

Fig. 10. Scattering parameters of the filter shown in Fig. 9 (Load curves). Results for the filter without the dielectric posts are also included to show the loading effect of the posts.

in Fig. 7 that in this region the images series converges very fast, and it is therefore preferred over the Kummer technique. Using this novel strategy, a very efficient formulation of the surface IE has been implemented.

III. Results

To show the validity and flexibility of the IE technique just presented, we have investigated two inductive microwave waveguide filters of practical interest. For comparative purposes, all CPU times included in this section have been obtained in a PC computer with a 3 GHz CPU processor.

The first structure investigated is an inductively coupled rectangular waveguide filter with reduced dimensions, due to the use of dielectric posts inside the cavities (see Fig. 9). The typical rounded corners mechanization effects, attributed to low-cost milling manufacturing techniques, have also been considered (radius of curvature $R = 2.5$ mm). The results are presented in Fig. 10, together with HFSS© data, showing very good agreement with our new IE technique. For the simulation of this structure, we have used 178 basis functions, involving a

computational effort of 0.98 seconds per frequency point. The results obtained with HFSS© required a CPU time of 19.08 seconds per frequency point.

Finally, we have designed an evanescent rectangular waveguide filter composed of rectangular lossy dielectric posts (see Fig. 11). Inside the below cut-off waveguide of this structure, eight square dielectric resonators are coupled by proximity. Rounded corners are also considered during the mechanization of the below cut-off waveguide section as shown in Fig. 11 (radius of curvature $R = 2$mm). In Fig. 12

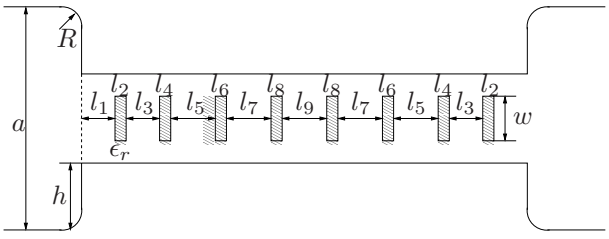

Fig. 11. Eighth order evanescent rectangular waveguide filter composed of square dielectric posts. The dimensions are: $a = 28.5$ mm, $w = 1.935$ mm, $h = 8.825$ mm, $\epsilon_r = 44$, $l_1 = 1.986$ mm, $l_2 = 0.899$ mm, $l_3 = 11.69$ mm, $l_4 = 0.951$ mm, $l_5 = 13.106$ mm, $l_6 = 0.95$ mm, $l_7 = 13.475$ mm, $l_8 = 0.95$ mm and $l_9 = 13.56$ mm, $R = 2$ mm.

we can observe the scattering parameters in the pass-band of the filter for several values of the dielectric loss tangent. As expected, the losses in the dielectric resonators essentially affect the insertion loss of the filter. In Table III we show the minimum insertion loss achieved inside the passband, for different values of the dielectric loss tangent.

It can be seen that the insertion loss can be kept below 0.5 dB if high quality dielectric resonators are used, with loss tangent values less than 0.0005.

For validation purposes, we compare these results with the ones provided by the commercial software HFSS©, for the case of $\tan(\delta) = 0.002$. A very good agreement is again obtained with the technique proposed in this paper.

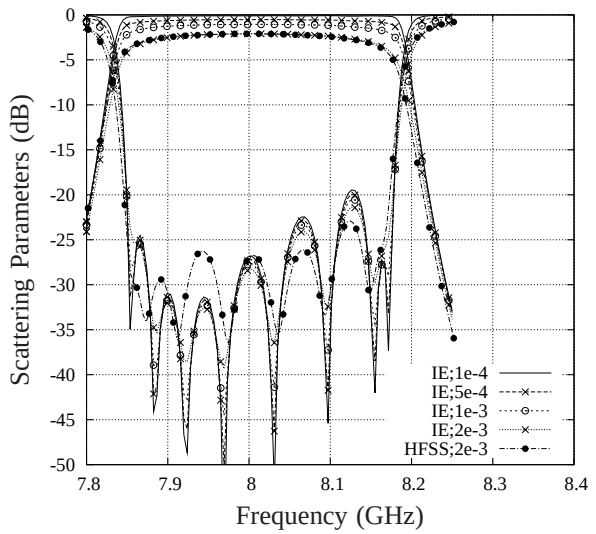

Fig. 12. In-band response of the filter shown in Fig. 11. Results provided by HFSS are included for comparison.

TABLE III
MINIMUM INSERTION LOSS WITHIN THE PASSBAND FOR DIFFERENT VALUES OF THE DIELECTRIC LOSS TANGENT.

$\tan(\delta)$	Insertion Loss (dB)
0.0001	0.10
0.0005	0.52
0.001	1.05
0.002	2.10

In particular, both numerical techniques predict exactly the same minimum insertion loss within the passband (2.1 dB for the case of $\tan(\delta) = 0.002$). For the analysis of this evanescent waveguide filter, we have used 340 basis functions for segmenting the whole geometry. Our software tool has only taken 2.6 seconds per frequency point to complete the analysis, whereas the commercial software HFSS© did require 39.6 seconds per frequency point to obtain the results with a similar degree of accuracy.

ACKNOWLEDGMENTS

The authors would like to thank Alcatel Alenia Space (Madrid, Spain) for having provided data of the lossy dielectric loaded evanescent waveguide filter. They also wish to acknowledge the economic support of MEC, Spanish Government, through the coordinated Research Project TEC2004/04313-C02.

IV. CONCLUSIONS

In this paper, a surface IE technique, based on the PPW Green functions, has been employed for the accurate and efficient analysis of arbitrarily shaped inductive obstacles placed within rectangular waveguides. To speed up the analysis tool, a deep study on the convergence properties of the Green functions and their derivatives has been performed. Such study has led to a novel strategy which combines the spatial series with the Kummer transformation applied to the spectral series. In the paper, several inductive filtering topologies of practical interest have been demonstrated using the new proposed technique.

APPENDIX I
KUMMER TRANSFORMATION FOR GREEN FUNCTIONS

The Kummer transformation is based on the extraction of the asymptotic term of the series to be evaluated. Once extracted, the asymptotic term must be computed analytically. The extraction of the asymptotic term of the spectral series for the magnetic vector potential Green function can be found in [22]. For the formulation presented in this work, we also need to accelerate the magnetic scalar potential Green function shown in Table I. After some manipulations, the asymptotic

term can be obtained in closed form as follows:

$$\sum_{n=1}^{\infty} \frac{j\,a}{n\,\pi}\,\cos\Big(\frac{n\pi}{a}x\Big)\cos\Big(\frac{n\pi}{a}x'\Big)\,e^{-j(n\pi/a)\,|z-z'|} = -\frac{j\,a}{2\pi}\,\mathrm{Re}\Big\{\ln\big[(1-\mathrm{D})\,(1-\mathrm{C})\big]\Big\} \tag{13a}$$

$$C = \exp\left\{j\frac{\pi}{a}\Big[(x-x') + j|z-z'|\Big]\right\},$$

$$D = \exp\left\{j\frac{\pi}{a}\Big[(x+x') + j|z-z'|\Big]\right\}. \tag{13b}$$

In [22], the Kummer transformation is also applied to calculate some of the derivatives needed in the present formulation, as shown in Table II. In particular, in [22], we find the asymptotic terms for the x and z derivatives of the magnetic vector potential ($G_A^{(ext)}$). Using the present formulation, we also need to evaluate in closed form the asymptotic term for the x-derivative of the magnetic scalar potential ($G_W^{(ext)}$). With the results presented in [22] this is a simple task, leading to:

$$\sum_{n=1}^{\infty} \sin\Big(\frac{n\pi}{a}x\Big)\cos\Big(\frac{n\pi}{a}x'\Big)\,e^{-j(n\pi/a)\,|z-z'|} = \frac{1}{2}\,\mathrm{Im}\left\{\frac{\mathrm{D}'-\mathrm{C}'}{(1-\mathrm{C}')\,(1-\mathrm{D}')}\right\} \tag{14a}$$

$$C' = \exp\left\{j\frac{\pi}{a}\Big[(x'-x) + j|z-z'|\Big]\right\},$$

$$D' = \exp\left\{j\frac{\pi}{a}\Big[(x+x') + j|z-z'|\Big]\right\}. \tag{14b}$$

The asymptotic terms required in our formulation are now analytically evaluated using the expressions shown in (13) and (14), together with those given in [22].

REFERENCES

[1] Y.-C. Shih, "Design of waveguide E-plane filters with all metal inserts," IEEE Transactions on Microwave Theory and Techniques, vol. 32, no. 7, pp. 695–704, July 1984.

[2] G. Conciauro, P. Arcioni, M. Bressan, and L. Perregrini, "Wide-band modeling of arbitrarily shaped H-plane waveguide components by the "boundary integral-resonant mode expansion method"," IEEE Transactions on Microwave Theory and Techniques, vol. 44, no. 7, pp. 1057–1066, 1996.

[3] M. Guglielmi, P. Jarry, E. Kerherve, O. Roquebrun, and D. Schmitt, "A new family of all-inductive dual-mode filters," IEEE Transactions on Microwave Theory and Techniques, vol. 49, no. 10, pp. 1764–1769, October 2001.

[4] V. E. Boria, M. Bozzi, D. Camilleri, A. Coves, H. Esteban, B. Gimeno, M. Guglielmi, and L. Polini, "Analysis and design of all-inductive filters with dielectric resonators," in 33rd Microwave Conference, Munich, Germany, 7-9, October 2003, pp. 1247–1250, vol.3.

[5] T. Toyama and E. Sawado, "Functionals in the variational method applied to equivalent impedance matrix of metallic posts unsymmetrically positioned in a rectangular waveguide," IEEE Transactions on Microwave Theory and Techniques, vol. 40, no. 8, pp. 1655–1660, August 1992.

[6] R. R. Mansour and R. H. Macphie, "An improved transmission matrix formulation of cascaded discontinuities and its application to E-plane circuits," IEEE Transactions on Microwave Theory and Techniques, vol. 34, no. 12, pp. 1490–1498, December 1986.

[7] J. M. Reiter and F. Arndt, "Rigorous analysis of arbitrarily shaped H- and E-plane discontinuities in rectangular waveguides by a full-wave boundary contour mode-matching method," IEEE Transactions on Microwave Theory and Techniques, vol. 43, no. 4, pp. 796–801, April 1995.

[8] H. Esteban, S. Cogollos, V. Boria, A. A. San Blas, and M. Ferrando, "A new hybrid mode-matching/numerical method for the analysis of arbitrarily shaped inductive obstacles and discontinuities in rectangular waveguides," IEEE Transactions on Microwave Theory and Techniques, vol. 50, no. 4, pp. 1219–1224, April 2002.

[9] T. Rozzi, F. Moglie, A. Morini, W. Gulloch, and M. Politi, "Accurate full-band equivalent circuits of inductive posts in rectangular waveguide," IEEE Transactions on Microwave Theory and Techniques, vol. 40, no. 5, pp. 1000–1009, May 1992.

[10] Y. Leviatan, P. G. Li, A. T. Adams, and J. Perini, "Single post inductive obstacle in rectangular waveguide," IEEE Transactions on Microwave Theory and Techniques, vol. 31, no. 10, pp. 806–812, October 1983.

[11] P. G. Li, A. T. Adams, Y. Leviatan, and J. Perini, "Multiple post inductive obstacles in rectangular waveguide," IEEE Transactions on Microwave Theory and Techniques, vol. 32, no. 4, pp. 365–373, April 1984.

[12] H. Auda and R. F. Harrington, "Inductive posts and diaphragms of arbitrary shape and number in a rectangular waveguide," IEEE Transactions on Microwave Theory and Techniques, vol. 32, no. 6, pp. 606–613, June 1984.

[13] C.-I. G. Hsu and H. A. Auda, "Multiple dielectric posts in a rectangular waveguide," IEEE Transactions on Microwave Theory and Techniques, vol. 34, no. 8, pp. 883–891, August 1986.

[14] R. Gesche and N. Löchel, "Two cylindrical obstancles in a rectangular waveguide-resonances and filter applications," IEEE Transactions on Microwave Theory and Techniques, vol. 37, no. 6, pp. 962–968, June 1989.

[15] F. Alessandri, M. Chiodetti, A. Giugliarelli, D. Maiarelli, G. Martirano, D. Schmitt, L. Vanni, and F. Vitulli, "The electric-field integral-equation method for the analysis and design of a class of rectangular cavity filters loaded by dielectric and metallic cylindrical pucks," IEEE Transactions on Microwave Theory and Techniques, vol. 52, no. 8, pp. 1790–1797, August 2004.

[16] V. Catina, F. Arndt, and J. Brandt, "Hybrid surface integral-equation/mode-matching method for the analysis of dielectric loaded waveguide filters of arbitrary shape," IEEE Transactions on Microwave Theory and Techniques, vol. 53, no. 11, pp. 3562–3567, November 2005.

[17] A. F. Peterson, S. L. Ray, and R. Mittra, Computational Methods for Electromagnetics. IEEE Press, 1998, p. 451.

[18] J. R. Mosig, Integral Equation Technique. New York: Wiley Interscience Publication, 1989.

[19] A. J. Poggio and E. K. Miller, Integral Equation Solutions of Three-dimensional Scattering Problems. Oxford: Pergamon Press, 1973.

[20] C. A. Balanis, Advanced Engineering Electromagnetics. John Wiley and Sons, 1989.

[21] R. E. Collin, Field Theory of Guided Waves. Piscataway, N.J.: IEEE Press, 1991.

[22] Y. Leviatan and G. S. Sheaffer, "Analysis of inductive dielectric posts in rectangular waveguide," IEEE Transactions on Microwave Theory and Techniques, vol. 35, no. 1, pp. 48–59, January 1987.

[23] F. Capolino, D. R. Wilton, and W. A. Johnson, "Efficient computation of the 2-D Green's function for 1-d periodic structures using the ewald method," IEEE Transactions on Antennas and Propagation, vol. 53, no. 9, pp. 2977–2984, September 2005.